

Experiment exposing refractory metals to impacts of 440 GeV/c proton beams for the future design of the CERN antiproton production target: Experiment design and online results

Claudio Torregrosa Martin,^{1,2,*} Antonio Perillo-Marcone,¹ Marco Calviani,¹ Luca Gentini,¹ Mark Butcher,¹ and José-Luis Muñoz-Cobo²

¹CERN, 1211 Geneva 23, Switzerland

²Universidad Politécnica de Valencia, Camino de Vera s/n, Valencia, Spain



(Received 12 November 2018; published 7 January 2019)

The HRMT27-RodTarg experiment employed the HiRadMat facility at CERN to impact intense 440 GeV proton beams onto thin rods 8 mm in diameter, 140 mm in length, and made of high-density materials such as Ir, W, Ta, Mo, and alloys. The purpose of the experiment was to reduce uncertainties on the CERN antiproton target material response and assess the material selection for its future redesign. The experiment was designed to recreate the extreme conditions reached in the production target, estimated in an increase of temperature above 2000 °C in less than 0.5 μ s and a subsequent compressive-to-tensile pressure wave of several gigapascals. The goals of the experiment were (i) to validate the hydrocode calculations used for the prediction of the antiproton target response and (ii) to identify limits and failure mechanisms of the materials of interest. In order to accomplish these objectives, the experiment relied on extensive instrumentation (pointing at the target rod surfaces). This paper presents a detailed description of the experiment as well as the recorded online results which showed that most of the investigated materials suffered internal damage from conditions 5–7 times below the ones present in the AD target. Tantalum, on the other hand, apparently withstood the most extreme conditions without presenting internal cracking.

DOI: [10.1103/PhysRevAccelBeams.22.013401](https://doi.org/10.1103/PhysRevAccelBeams.22.013401)

I. INTRODUCTION

Antiprotons are currently produced at CERN by impacting 26 GeV/c proton beams with a fixed target, called the AD target, which consists of a water-cooled assembly whose core is made of a 3-mm-diameter, 55-mm-long iridium rod. The characteristics of antiproton production require a compact target in order to avoid antiproton reabsorption in the surrounding material and to be as close as possible to a punctual source for the downstream collector system [1,2]. For this reason, a thin rod made of a high-density material (such as iridium) and a focused primary proton beam have to be used. During the interaction of the proton beam with this high-density material, extremely high and fast depositions of energy take place, with a subsequent rapid rise of the temperature and thermal and mechanical loads. It is estimated that a single proton pulse impact—composed by 1.5×10^{12} ppp (protons per pulse) and a spot size of 0.5×1 mm at 1σ —leads to a

rise of the temperature above 2000 °C in the core and successive dynamic pressure waves on the order of several gigapascals.

The current AD-target design as well as the configuration of the target area dates back to the 1980s. An upgrade of the area is planned to take place during the CERN long shutdown 2 (2019–2020), which, among other activities, will involve a redesign of the antiproton target to guarantee the next decades of antiproton physics at CERN. In this context, R&D activities have been triggered for the proposal of an optimized new design. One of them is the application of numerical tools, such as hydrocodes, to the resolution of the extreme dynamic conditions reached in the target core [3]. These numerical studies showed that a radial mode of vibration is excited as a consequence of the sudden deposition of energy in the target material, exposing it to oscillating compressive-to-tensile stresses well above its strength limit. Simulations also identified that the origin of this compressive-to-tensile response was a constructive interference between generated end-of-pulse tensile waves and the natural radial wave, bringing to light the importance of the pulse length in the dynamic response at these conditions.

The performed hydrocode simulations also included failure models, which can take into account the material limits when a given threshold (depending on the used

*claudio.torregrosa@cern.ch

Published by the American Physical Society under the terms of the *Creative Commons Attribution 4.0 International* license. Further distribution of this work must maintain attribution to the author(s) and the published article's title, journal citation, and DOI.

failure model) is exceeded. The implementation of these models predicted that a large fraction of the target core may fracture from the very first pulse impact. This fracture can be an important operation issue, since eventually it can lead to a loss of effective density of the target material and therefore a reduction of the beam-target interaction and antiproton production.

Nevertheless, it also is important to point out that the performed numerical studies of Ref. [3] suffer from intrinsic limitations; simulations can go only as far as the constitutive models of the materials used, and, in that sense, the numerical studies described rely on noteworthy assumptions. The availability of material strength models at high strain rates (most of them obtained experimentally by Hopkinson bar tests [4]) is limited to regimes of relatively low temperatures, well below the 2000°C reached in the core. A dedicated dynamic characterization of pure iridium at high temperatures by using Hopkinson bar tests was carried out to extract the material models necessary for this project [5]. However, the maximum temperature reached in these tests was only 1250°C. Thus, a partial extrapolation of the strength model in the hydrocode simulations is required. Furthermore, the failure mechanisms and limits need to be identified experimentally in order to be properly implemented in the code, which is not the case for the simulations of Ref. [3], where the applied failure thresholds are extracted from experiments with load conditions different from the ones present in the AD-target core.

For these reasons, it was considered that an experiment was necessary to answer the following questions: (i) What really happens to the target core material exposed to these extreme dynamic conditions and high tensile pressure loads induced by a beam impact? (ii) Which are the main or the different mechanisms of failure? (iii) What is the effect of this failure in the material effective density and therefore antiproton production (due to the reduction of beam-target material interaction)? (iv) Is there another high-density material that behaves better than the ones numerically studied?

The HiRadMat facility [6], in operation at CERN since 2012, uses one of the extraction lines of the Super Proton Synchrotron (SPS) and is capable of providing intense proton beams from the SPS with a momentum of 440 GeV/*c* and a wide flexibility of intensities and beam optic parameters to test accelerator equipment. Hence, an experiment using this facility was designed for recreating equivalent conditions as the ones present in the AD-target core, following two main goals: (i) cross-check and validation of the numerical hydrocodes employed for simulating the material response of the antiproton target core presented in Ref. [3] and (ii) gaining experimental insights in the targets' response and assessing the selection of the future antiproton target material. Different high-*Z* candidate materials such as W, Ir, Mo, or Ta were irradiated so quantitative and qualitative comparison between their performance can be obtained.

This study presents the particularities of the experimental design and most relevant online results recorded. Postirradiation examinations (PIEs), together with numerical simulations and experimental result comparisons, will be presented in another paper.

II. DESIGN OF THE EXPERIMENT

The HRMT27-RodTarg experiment aimed at accurately impacting high-energy and intense proton beams onto very thin targets and, at the same time, recording the phenomena at their surfaces, which takes place in the order of microseconds. This task involves several technical challenges that had to be overcome, starting from the design of the targets in which conditions equivalent to the ones present in the AD target had to be recreated and, at the same time, produced responses at their periphery (such as reached velocities and temperatures) that are below the instrumentation limitations. Another challenge was the required accuracy on the impact position and beam monitoring, since, to obtain the numerically predicted radial wave, it was fundamental that the beam hits the center of the targets. The third challenge involved the selection of the instrumentation, which had to be compatible with a harsh environment, such as temperature variations (the target surface could reach up to 900°C), velocities and inertia forces on the target surfaces (40 m/s and 10⁸ m/s²), and high levels of prompt radiation produced as a consequence of the high-density materials employed as targets.

A. Design of the targets and beam parameter selection

The target geometry and beam parameter selection was the first step in the experiment design. The HiRadMat facility receives proton beams from the SPS at 440 GeV/*c*, while the AD target receives the beam from the PS at 26 GeV/*c*. Fortunately, the SPS can provide a beam to the HiRadMat facility with some flexibility regarding the beam intensity, spot size, and pulse length (but not in the energy). Hence, to recreate equivalent AD-target conditions in the controlled environment of HiRadMat, it was necessary to adjust these beam parameters, together with the target geometry.

The first aspect deduced during the initiation of the target design process was the need of scaling. A 3-mm-diameter rod, as in the real AD-target core, would not have been practical for several reasons; first of all, the fixed momentum of 440 GeV/*c* of the HiRadMat proton beam required us to increase the diameter of the incident beam to achieve energy depositions and temperatures representative of the ones in the AD target. The required defocusing of the HiRadMat beam can be observed in Fig. 1, in which the maximum energy density deposited as a function of the target length is plotted for the 26 GeV/*c* beam of the AD target (red curve) and the 440 GeV/*c* of HiRadMat (blue curve), considering a beam spot size of 1.5 × 1.5 mm at 1σ

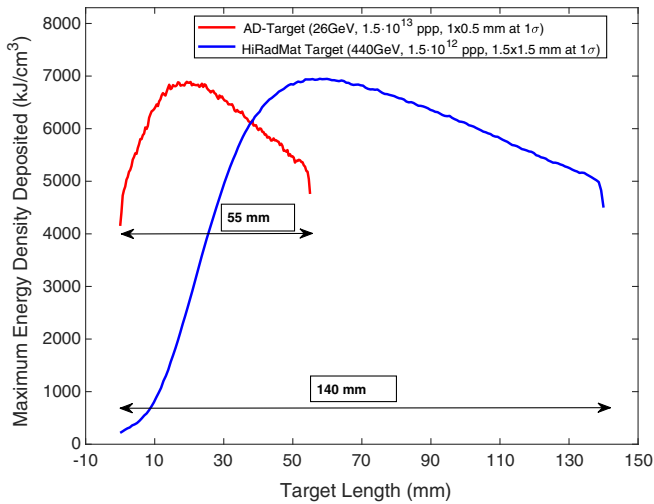


FIG. 1. Plot of the maximum energy density deposited as a function of the target length for the AD-target beam (26 GeV/ c) and HiRadMat beam (440 GeV/ c) calculated by means of FLUKA [7] Monte Carlo simulations. The length 0 in the plot corresponds to the upstream extremity of the target.

for the latter. The plot shows that, with the selected intensity, a beam spot size 3 times larger than in the AD target is required in HiRadMat for reaching an equivalent maximum energy density deposition.

The requirement of the defocusing of the HiRadMat beam led to the conclusion that the rod diameter had to be increased as well to get an equivalent beam-to-target-radius ratio. In addition, this increase in the target diameter was convenient from an instrumentation point of view, as it was shown via simulations that, by making the target thinner, the velocity reached on the surface increases above the instrumentation limitation. A rod diameter of 8 mm, as shown in Fig. 2, was selected as a compromise. Together with this diameter, the pulse length was selected in order to excite the radial mode of vibration in such a way that the compressive-to-tensile pressure response present in the AD target takes place [3]. This pulse length was found in $0.9 \mu\text{s}$ (composed of 36 bunches spaced by 25 ns), which corresponds to the duration of approximately half of the period of the 8-mm-diameter rod radial mode.

The lengths of the targets were selected conditioned by the fact that a 440 GeV/ c proton beam would have a significantly different longitudinal profile of deposited energy than that of a 26 GeV/ c beam (as shown in Fig. 1). The density of the irradiated materials also played an extra role in the length selection in order to have an equivalent longitudinal profile of deposited energy in all the targets. Based on that, a length of 140 mm for the targets of tungsten and iridium was selected, 170 mm for the tantalum, and 240 mm for the molybdenum and TZM.

Figure 3 shows a comparison between the temperature profile reached in the AD target (up) and in the HiRadMat target (down) for the HiRadMat proton beam parameters

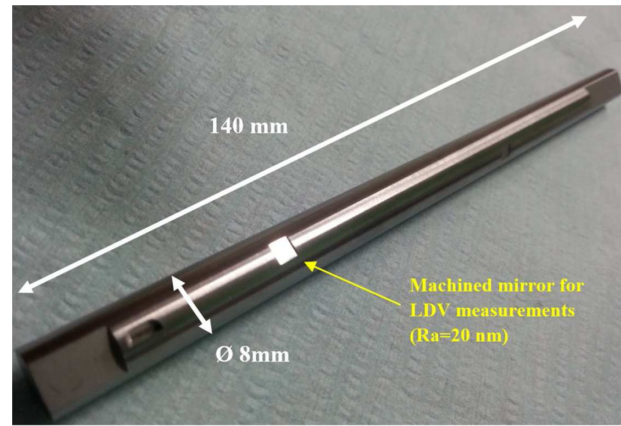


FIG. 2. Picture of the tungsten target showing one of the multiple mirrors machined on its surface, where the laser Doppler vibrometer (LDV) was pointed in order to measure its vibration when impacted by the proton beam.

selected (1.5×10^{12} ppp with a beam size of 1.5×1.5 mm at 1σ). This comparison is carried out assuming tungsten as the target material for both rods. It can be observed in the figure how, with these beam parameters, the adiabatic rise of temperature in both targets is quite similar, reaching a maximum around $2000 \text{ }^\circ\text{C}$ in the bulk material and a temperature difference from the center to the periphery close to $1800 \text{ }^\circ\text{C}$. This comparison of the reached temperature in the HiRadMat target versus AD-target core, even if done assuming tungsten as the material, can be perfectly extrapolated to every other tested material (iridium, molybdenum, tantalum, etc.).

Figure 4 shows a comparison of the pressure response simulated by hydrocodes in the AD-target core (left) and the HRMT27 experimental target (right). These simulations are considering a Johnson-Cook (JC) strength model [8], which take into account the material response beyond plastic deformation, but a failure model of the material is not included (so the waves can be easily compared).

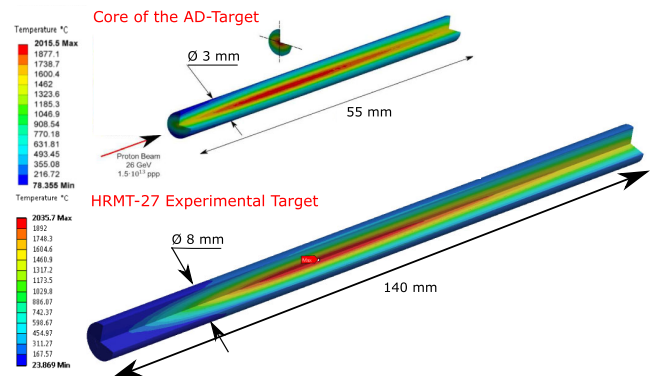


FIG. 3. Comparison between the estimated temperature reached in the AD target (top) and in the designed HiRadMat targets (bottom), assuming tungsten in both targets.

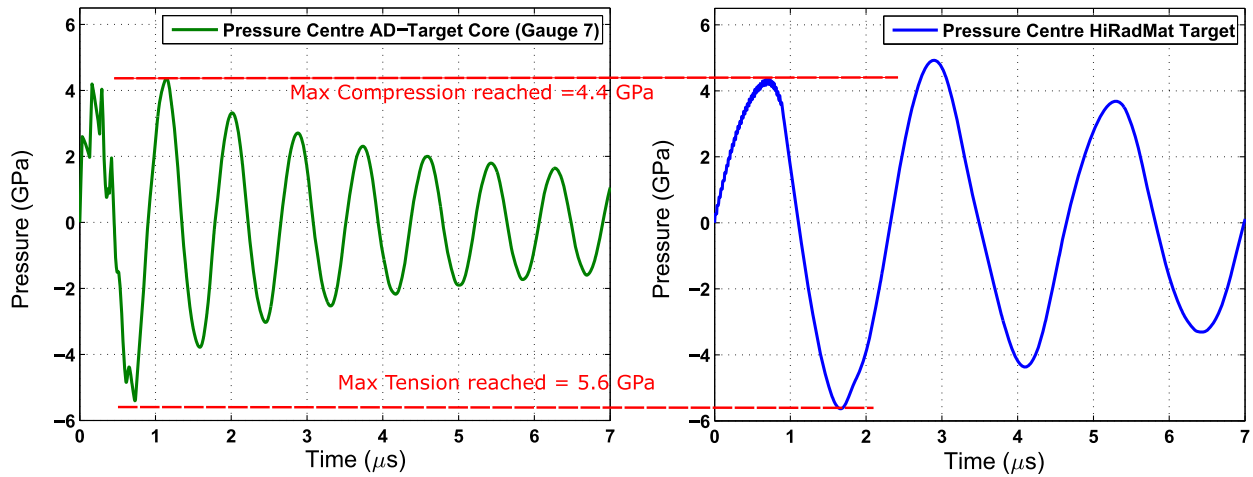


FIG. 4. Comparison of the simulated pressure response in the center of the AD-target core (left) and the HRMT27 experimental target (right), showing the emulation of equivalent AD-target tensile pressures in the latter.

More details on this type of simulations and the material models employed can be found in Ref. [3]. As can be seen in the figure, with the selected beam parameters and target geometry, a radial compressive-to-tensile pressure wave also takes place in the HiRadMat target due to the end-of-pulse tensile wave amplification phenomenon, achieving equivalent conditions as in the AD target. A pressure of 4.4 GPa is expected in compression and -5.6 GPa in tension for the case where W is considered as the target material. The main difference is in the radial period of the wave produced HiRadMat, which is expected to be around $\sim 2.3 \mu\text{s}$ instead of the $\sim 0.8 \mu\text{s}$ of the AD-target core, due to the larger rod diameter of the experimental target.

1. Expected velocity response on the target surface

Figure 5 shows the expected surface radial velocity of the experimental target periphery at the longitudinal region where the largest amount of energy is deposited. In red, the simulation does not consider a failure model, while in blue, the minimum hydrostatic pressure failure model for tungsten is considered (similarly as in Ref. [3]). As can be seen in the picture, velocities above 40 m/s are expected in both cases.

The interesting feature of the comparison between the simulations of Fig. 5 is the evident change in the velocity response when failure is considered. In the latter, the internal fracture would take place in the first negative oscillation of the pressure wave. This simulated fracture is shown in the contour plot in Fig. 6, where the failure of the target in these conditions is presented. As a consequence of this fracture, the radial wave is damped after a few oscillations, presenting as well a period reduction induced by the change of effective radial distance of travel of the wave due to the portion of cracked material in the inner regions of the target. This change in the response and distortion of the radial wave will be useful for interpretation purposes during the experiment to help identifying when,

and in which conditions, an internal fracture of the irradiated targets was taking place.

2. Selection of points of measurement and mirror roughness requirements

Even if the conditions reached in the AD target were recreated with the experimental target of the geometry

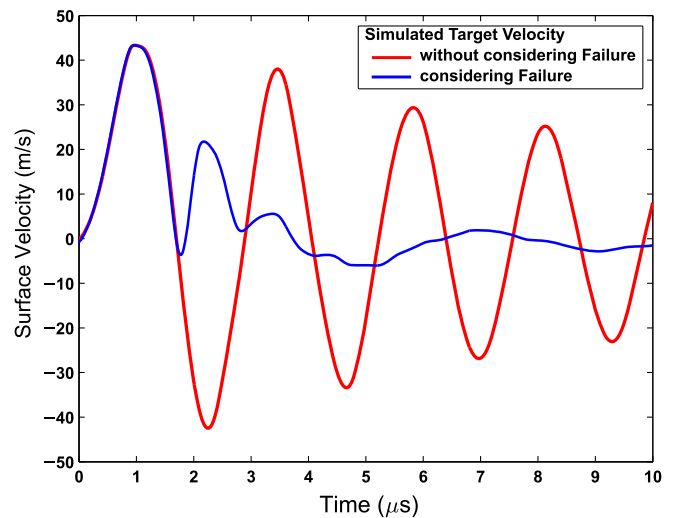


FIG. 5. Comparison of the simulated surface velocity when reaching AD-target conditions in the experimental targets. Without considering a failure model (red curve) and considering a failure model (blue curve).



FIG. 6. Estimation of failure of a tungsten HRMT27 target at conditions reached in the AD-target core assuming W and a minimum hydrostatic pressure failure model with a failure threshold of 2.6 GPa.

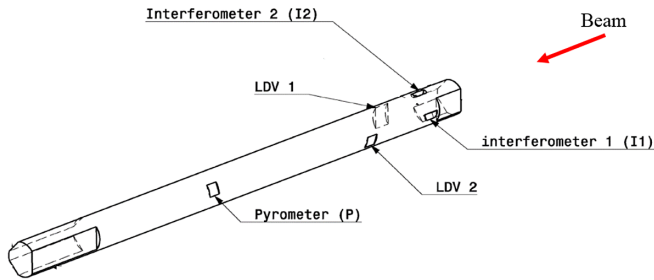


FIG. 7. Isometric view of the 140-mm-long targets, indicating the points of measurement for the different optical instruments used in the experiment.

presented in the previous section, there is an additional requirement that had to be fulfilled, such as being able to actually measure the vibrations of the targets. The expected velocities reached at some points of the target surface were so high (well above 40 m/s) that, in order to avoid saturation of the instruments, the selection of measurement points had to be done very carefully. Figure 7 shows the measurement points selected after several iterations and cross-checks with simulations. As can be seen in the figure, all the measurement points of velocity and displacement are placed close to the upstream end of the target, where velocities are considerably lower (below the 24 m/s instrumentation limitation) than in the longitudinal center of the target. For the LDV measurements, simple flat surfaces (mirrors) were machined (LDV 1 and LDV 2 in Fig. 7), whereas for the interferometer measurements (2 m/s velocity limitation), small slots on the target surface were machined in such a way that the surface of measurement forms a 30° angle with the radius of the target. It can be shown with simulations that the inclusion of these inclined surfaces slightly modifies the radial mode of vibration of the rod (together with a velocity projection in that plane), which results in a speed reduction of more than one order of magnitude in this point of measurement. Nevertheless, it shall be noticed that all the results presented in this paper correspond to LDV measurements, which were significantly less noisy than the interferometer ones. Hence, they are not subjected to this modification in the inclined surfaces.

A V-shaped support in the target sample holder, as will be described in Sec. II B, provided its precise angular positioning, since these small surfaces had to be perfectly perpendicular to the interferometer optical head, as shown in Fig. 11.

Another crucial requirement for the target specification was the mirror roughness. It was observed in the simulations that, due to the triaxial nature of the material expansion and the induced modal vibrations, the exact points to which the optical instruments were aiming would also move and oscillate in the longitudinal direction. This would result in a longitudinal displacement of the point of measurement, with a frequency corresponding to the one of

the radial wave. This circumstance brought up the concern that, if the surface roughness is of the order of magnitude of the radial wave to be measured (which had an estimated amplitude of approximately $0.4 \mu\text{m}$ in the low-intensity pulses) and the point of measurement changes, then the consequence would be that only the surface roughness would be spuriously measured instead of the desired radial displacement.

The only solution that was conceived to minimize these uncertainties was to reduce the roughness of the surface of measurement as much as possible. A roughness of $R_a = 20 \text{ nm}$ in the mirrors was achieved by fine polishing techniques using microdiamond powders.

B. General layout of the experiment

The experiment was designed in a modular way in order to facilitate the mounting and dismounting procedure according to the “as low as reasonably achievable” principle to minimize radiation exposure. Figure 8 shows a CAD model of the experiment’s full assembly.

The experiment counted on a vacuum tank with a 610 mm height, a 500 mm length, and a 420 mm width, which involved two visual portals made with radiation-resistant glass to avoid their darkening during the experiment [9]. It also included two 0.254-mm-thick Be windows for the inlet and outlet of the proton beam and five vacuum compatible feedthroughs for the in-tank instrumentation.

The tank was placed on top of motorized experimental tables. These tables provided remote-controlled horizontal and vertical degrees of freedom to move the vacuum tank for the targets’ alignment with the incoming beam. Specifically designed beam position monitors BPKG and BTV (stripline pick-up beam position monitor working in air [10] and beam TV [11]) were attached to the upstream part of the tank. The signals given by these monitors when sending pilot pulses were used as a reference for the alignment before the target irradiation. The BTV also provided online information about the beam parameters on target during the experiment, such as the position (with a

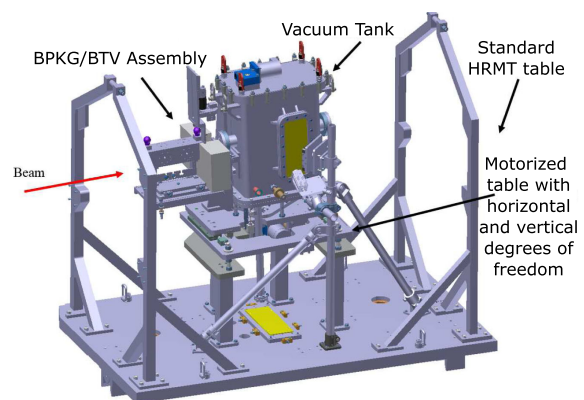


FIG. 8. 3D model of the full HRMT27 experiment.

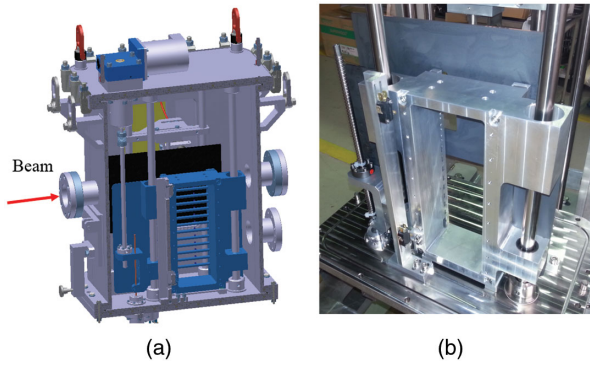


FIG. 9. (a) Inner view of the vacuum tank, including the mobile sample holder made of aluminum (blue). (b) Picture of the sample holder during assembling.

0.1 mm accuracy) and size, to be used for postexperiment simulations versus experimental data cross-checks. The movement of the experimental tables and the position control was carried out by step motors and linear variable differential transformer (LVDT) position sensors. The whole experimental setup was placed in a standard HiRadMat table (provided by the HiRadMat facility), which is compatible with the available space and multiple electrical and cooling connections of the facility. The table provides a quick plug-in system under its base in such a way that it can be dropped by a crane on the experimental position, enabling these electrical and water connections.

Inside the vacuum tank, 13 targets were placed in an aluminum sample holder which moved vertically during the experiment to put each corresponding rod in the on-beam position as shown in Fig. 9. The vertical movement of the sample holder was carried out by another step motor which was placed on top of the tank, together with an LVDT system. An empty space in the sample holder was added to allow the passage of pulses without interacting with any target during the alignment procedure or other possible configurations. In addition, this sample holder was used in the dismantling phase of the experiment, as it could easily be extracted from the top of the tank. In the sample holder, each target rod was clamped by small V-shaped graphite supports, which pressed the rods by means of springs as shown in Fig. 10. Inside the vacuum tank, four optical heads of the instrumentation were placed, pointing directly

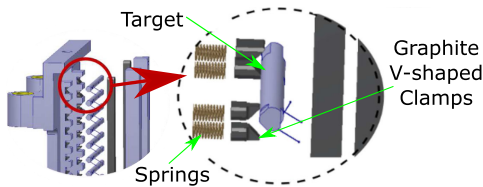


FIG. 10. Detailed view of the V-shaped clamping system of the targets in the sample holder. These V-shaped clamps were made of graphite and pressed the rods using small springs.

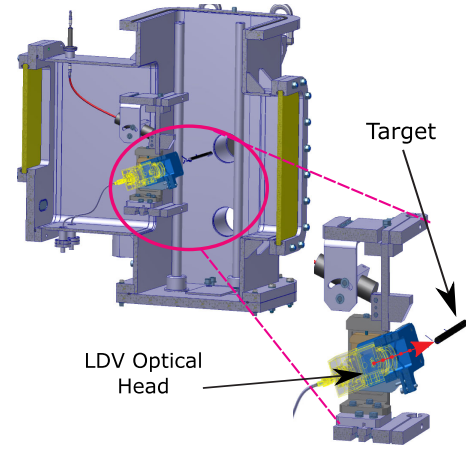


FIG. 11. Detailed view of the optical instrumentation placed inside the tank, pointing at the surface of the target on-beam position.

at the target on-beam position and the mentioned mirrors machined on its surface as shown in Figs. 11 and 12.

C. Instrumentation selection

As introduced in the previous section, the selection of the instrumentation was one of the most challenging tasks of the experiment. This was due mainly to the high prompt radiation close to the targets, as well as the huge temperature variations (up to 900 °C) and the inertia forces at their surfaces during the recording time. These specific challenges discouraged the use of strain gauges attached to the targets. Instead, it was concluded that the use of optical instrumentation (completely contactless) such as LDVs, interferometers, and pyrometers was the best possible solution.

Table I summarizes the selected instrumentation. All the instrumentation, except for the thermocouples, was not in contact with the target surfaces. These thermocouples,

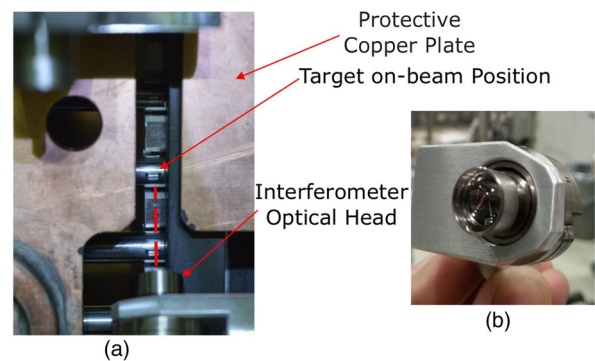


FIG. 12. (a) View of the target on-beam position from behind the interferometer head and through a water-cooled copper plate which protected the instrumentation from possible explosions. (b) Interferometer optical head.

TABLE I. Summary of all the instrumentation used in the experiment.

Instrument	Number	Measuring	Maximum resolution	Maximum range of measurement	Acquisition rate	Location
Interferometer heads Attocube FPS3010	2 heads	Displacement	80 nm	2 m/s	10 MHz	Inside the tank, pointing at the rod surface
LDV OptoMET®	1	Velocity and displacement	0.75 mm/s	24.5 m/s	10 MHz	Idem
Pyrometer IGA 740-LO	1	Temperature	0.02 °C	300–1400 °C	4 MHz	Idem
Thermocouples (type K)	26 (2 per target)	Temperature	10 °C	1500 °C	80 Hz	Attached to the targets
LDV Polytec®	1	Velocity and displacement	0.73 mm/s	24 m/s	10 MHz	In the bunker of the adjacent tunnel
Radiation hard camera [12]	2	Video	400 TVL	...	25 fps	Outside the tank
HD camera [13]	1	Video	1080p	...	25 fps	Outside the tank
Pirani pressure gauge	1	Pressure	...	10 ⁻³ mbar	80 Hz	Inside the tank

which had a much lower acquisition rate, were mainly used to monitor the temperatures during the experiment, since they were not able to record the adiabatic increase of temperature on the target surface as a consequence of the beam impact.

No active electronics were placed close to the tank. The recorded signals measured by the passive optical heads pointing at the target on beam position traveled through optic fibers to the conditioning electronics and a National Instrument®PXI-based data acquisition system, which was remotely placed in a shielded bunker situated in a tunnel adjacent to the facility.

Outside the tank, and attached to the standard HiRadMat table, a supporting structure was placed holding a radiation hard camera and a high-definition (HD) camera, which pointed to the interior of the tank to monitor the experiment through one of the visual portals made of radiation-resistant glass.

D. List of investigated target materials

Table II shows the list of the 13 targets irradiated in the experiment and their density and length, together with a picture of the sample holder, which shows the respective targets. The order of the targets in the table is consistent with the position of each of them in the sample holder. The selection of these target materials was done based on possible candidates for the future AD target. Apart from the pure materials, some alloys or doped materials were added to the experiment such as W-La and TZM. All of the targets were machined starting from rods with an 8 mm diameter. The next paragraphs explain the reasons behind the selection of these materials and details of their manufacturing process.

Iridium was included in the experiment due to the fact that this is the current target core material, selected by its high density in the last AD-target design in the late 1980s.

TABLE II. List of targets irradiated during the HRMT27 experiment.

Target no.	Target identifier	Material	Density (g/cm ³)	Target length [mm]	Picture of the 13 targets placed in the sample holder (same order of targets as rows in the table)
T13	W-Ta	Pure W clad in 2 mm Ta	...	140	
T12	Ir3	Pure Ir	22.4	140	
T11	Ir2	Pure Ir	22.4	140	
T10	Ir1	Pure Ir	22.4	140	
T9	W-La	W + La ₂ O ₃	19.3	140	
T8	W3	Pure W	19.3	140	
T7	W2	Pure W	19.3	140	
T6	W1	Pure W	19.3	140	
T5	Ta2	Pure Ta	16.6	170	
T4	Ta1	Pure Ta	16.6	170	
T3	TZM2	Mo-Ti-Zr Alloy	10.2	240	
T2	TZM1	Mo-Ti-Zr Alloy	10.2	240	
T1	Mo	Pure Mo	10.2	240	

The raw material for this target was provided by Goodfellow [14]. The rod was manufactured from a drip-melted ingot by electron beam melting. The drip-melted ingot was then forged and swaged into the rod diameter.

Pure tungsten was included due to its high density and due to the experience and interest in this material in the scientific community, in particular, as a candidate material for the divertor and the plasma-facing armor of the Tokamak fusion reactor of the International Thermonuclear Experimental Reactor or the Demonstration Power Station [15], as well as a target material for neutron spallation facilities [16–18]. Furthermore, the good availability of strength and failure models for tungsten and the fact that most of the hydrocode calculations applied to the AD target presented in Ref. [3] consider it as a core material supported its inclusion. For similar reasons, a target of pure tungsten doped with 1% of La_2O_3 was added. This oxide addition improves significantly the tungsten’s mechanical properties at a high temperature such as tensile and creep strength due to an increase of its recrystallization temperature [19]. Both pure tungsten targets and tungsten doped with 1% of La_2O_3 were provided by PLANSEE [20] and were produced starting from metal powder, pressed, sintered, and hot forged with stress-relieving heat treatment after hot working.

Molybdenum and TZM were selected despite their significantly lower density in order to assess the fact that they could have more chances to survive an equivalent AD-target beam impact, since the induced conditions would be less extreme. In addition, molybdenum and its alloys (such as TZM) are of interest for future R&D projects at CERN, such as target material for the potential beam dump facility [18]. Even if the significantly lower density of this material would affect the antiproton production if used in the AD target, this reduction could be partially compensated by an increase of the core length, which was the case for the copper targets used during the 1980s [21]. Molybdenum and TZM were provided by PLANSEE [20] and produced by sintering, hot forging, and a subsequent stress-relieving heat treatment.

Tantalum was included in the experiment given its high density, the extended research already existing for this material, and some specific mechanical properties. Dynamic properties of tantalum have been extensively studied, since it is a common material in shaped charge liners of warheads and explosively forged projectiles [22]. In addition, it has been reported in the literature that tantalum possesses a significantly high spall strength which can be of great interest for the AD-target core application [23] (spall strengths from 4 to 5 GPa were found in the range of strain rates reached in the AD-target core; 10^4 – 10^5 s^{-1} [24]). Furthermore, differently from the rest of the candidate materials, tantalum shows a very ductile behavior with a yield strength at room temperature of approximately 170 MPa and an ultimate tensile strength of 280 MPa, showing elongations to break above 30% [25].

Given that, due to the large levels of stresses taking place in the experiment, it is assumed that all of the target materials would experience plastic deformation in any case, it was considered very interesting to introduce tantalum in the experiment in order to compare possible failure mechanisms between materials with known different properties and ductility. The raw tantalum material was provided by PLANSEE [26], corresponding to its designated “Ta melting quality” (TaM). The rods were produced out of melted prematerial ingots, hammered, grounded, and delivered in nonannealed condition.

Finally, the last material included in the experiment was a tungsten target clad in tantalum. The presence of this target was motivated by the study presented in Ref. [3], in which it was numerically shown that the addition of a high-density cladding could effectively reduce the level of tensile pressures reached in the core of the AD target. Experimental proof of the success of this strategy was necessary, since in reality several uncertainties that are not taken into account by the simulations exist, such as the quality of the core-cladding interface and potential detachments due to the plastic deformation induced during irradiation. The 2-mm-thick Ta-clad tungsten target was manufactured by Advanced Technology & Materials Co. (AT&M) via a hot isostatic pressing process.

III. EXECUTION OF THE EXPERIMENT

Table III shows a summary of all the pulses impacted in the 13 targets. The first column of the table shows the seven irradiation intensities, in terms of total number of protons per pulse (ppp), together with the number of bunches which were composing each proton pulse. The bunch spacing was 25 ns for all the pulses, meaning that the pulses composed by 36 bunches had a total length of 0.9 μs . A total of 139 pulses were successfully impacted during the three days of experiment. The conditions reached in the targets varied from adiabatic increases of the temperature initially estimated at 65 °C, 110 °C, 130 °C, and 160 °C for Mo/TZM, Ta, W/WLa/W-Ta, and Ir, respectively, for the low-intensity pulses, while temperature increases up to approximately 800 °C, 1700 °C, 1900 °C, and 2000 °C for Mo/TZM, Ta, W/WLa/W-Ta, and Ir, respectively, were reached at the highest intensity.

As shown in the table, there were some targets such as T3-TZM1, T5-Ta2, T7-W2, and T11-Ir2 which were irradiated only up to intermediate intensities so the progressive damage in their bulk material during the postirradiation examination could be studied. It is important to note as well in the table that, after the irradiation at $\sim 7 \times 10^{11}$ ppp, all the targets were subjected to a second irradiation sequence at $\sim 2 \times 10^{11}$ ppp. The purpose of this step down in intensity was to try to infer online if internal damage on the targets was already taking place by comparing these responses with the ones recorded in the previous irradiation at 2×10^{11} ppp (before subjecting them to 5×10^{11} and 7×10^{11} ppp).

TABLE III. Summary of irradiation sequences and distribution of the 139 pulses during the experiment.

Intensity (ppp) No. bunches	Pulses per target												
	T1- Mo1	T2- TZM1	T3- TZM2	T4- Ta1	T5- Ta2	T6- W1	T7- W2	T8- W3	T9- WLa	T10- Ir1	T11- Ir2	T12- Ir3	T13- W-Ta
$\sim 1 \times 10^{11}$ single bunch	3	2	2	2	2	2	2	...	2	2	2	...	2
$\sim 2.1 \times 10^{11}$ 12 bunches	3	3	3	3	3	3	3	...	3	3	3	...	3
$\sim 5 \times 10^{11}$ 12 bunches	3	3	3	3	3	3	1	...	3	3	1	...	3
$\sim 7 \times 10^{11}$ 36 bunches	1	1	1	1	1	1	1	1	1
$\sim 2.1 \times 10^{11}$ 12 bunches	1	1	1	1	1	1	1	...	1	1	1	...	1
$\sim 9.2 \times 10^{11}$ 36 bunches	1	1	1	1	1	1	1	1	1
$\sim 1.3 \times 10^{12}$ 36 bunches	1	1	...	1	...	1	1	1	1
$\sim 1.5 \times 10^{12}$ 36 bunches	1	1	...	1	...	1	1	9	1	1	...	1	1

In addition, there were other targets such as T8-W3 and T12-Ir3 which were maintained unirradiated or “virgins” until the end of the experiment, when they were directly exposed to the maximum intensity. The purpose of this was to observe the response of these materials at extreme loads of AD-target condition without having previously been affected by lower-intensity pulses.

IV. EXPERIMENT ONLINE RESULTS

In the present section, online recorded data are selected and shown in such a way that a general picture of the behavior of all irradiated materials at the different exposed conditions can be extracted. In that sense, displacement and velocity data recorded mainly by the OptoMET® LDV are presented. These data are shown for the different irradiated materials classified in three different intensity ranges. (i) Low-intensity pulses, which correspond to impacted

pulses of only $\sim 1 \times 10^{11}$ ppp (first irradiation intensity). This intensity is on the order of ~ 15 times lower than the maximum irradiated intensity (at which equivalent AD-target conditions were expected). At this intensity, the response of some of the materials is still in the elastic regime. (ii) Medium- to high-intensity pulses, which correspond to impacted pulses from the second irradiation intensity, $\sim 2 \times 10^{11}$ ppp, from which significant changes in the response of some of the highest-density materials such as tungsten or iridium were already observed. (iii) High-intensity pulses, including particular cases in which AD-target equivalent conditions were impacted.

A. Dynamic response at low-intensity pulses $\sim 1 \times 10^{11}$ ppp

Figures 13(a) and 13(b) show the measured velocity by the LDV OptoMET® on a TZM target after an impact of

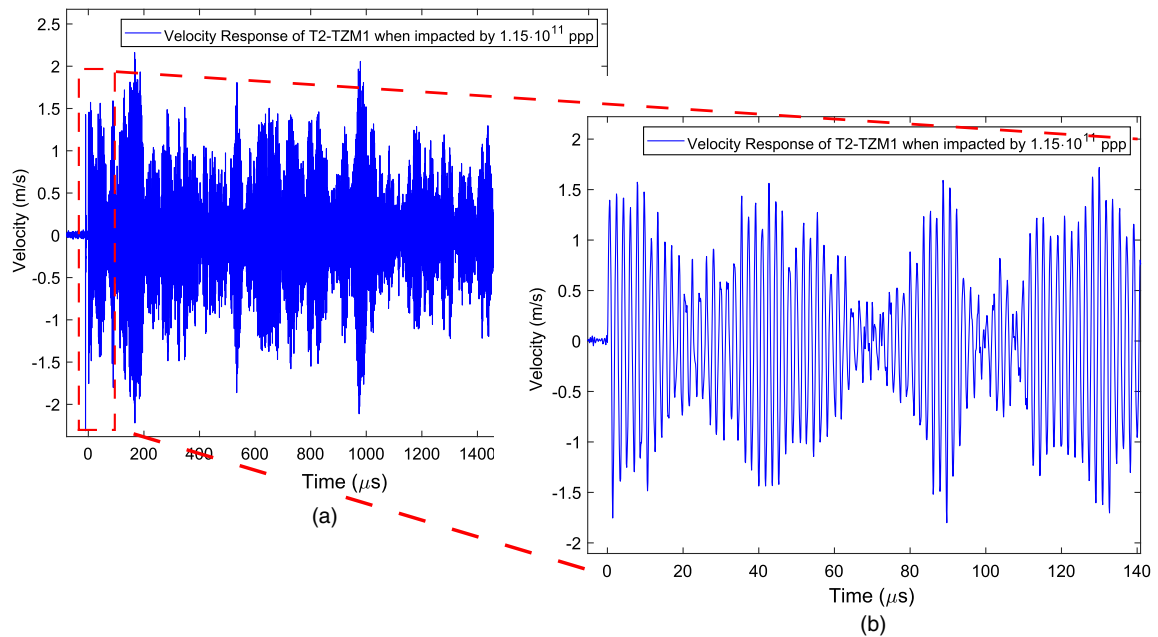


FIG. 13. Velocity at the surface of target T2-TZM1 when impacted by 1.15×10^{11} ppp (elastic regime) recorded by the LDV OptoMET®. (b) Enlargement of the first 140 μs where the radial wave can be observed.

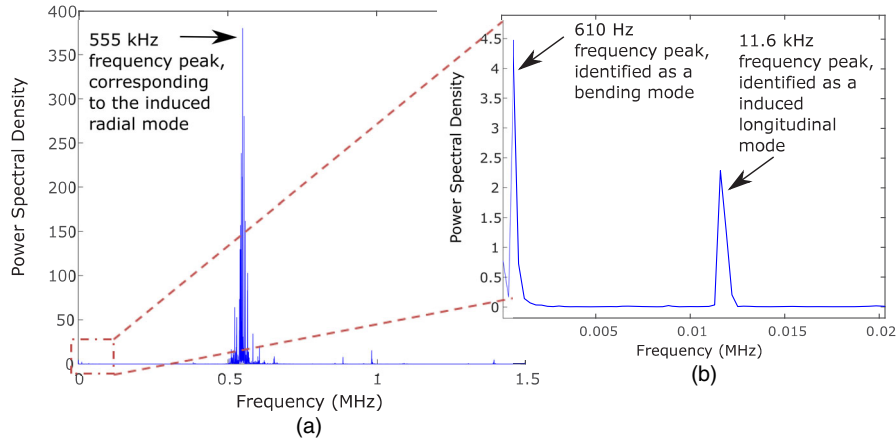


FIG. 14. (a) Plot of the frequency domain of the surface velocity of target T2-TZM1 when impacted by 1.15×10^{11} ppp (elastic regime). The plot shows how a radial mode with a frequency of 550 kHz dominates. (b) Enlargement of the lower-frequency range where two other modes can be appreciated, at 610 Hz (bending mode) and 11.6 kHz (longitudinal mode).

1.15×10^{11} ppp. The LDV was measuring within 3 ms after the impact. It is interesting to mention that the velocity response was not damped even after these 3 ms and thousands of oscillations of the radial mode, suggesting that the response of TZM at these conditions was still in the elastic regime. Figure 13(b) shows the velocity response during the first 140 μ s after the pulse impact, demonstrating that high-frequency radial modes with periods around 1.8 μ s dominate, as predicted by the simulations presented in Ref. [3].

This radial mode dominance can also be observed in Fig. 14(a), where a Fourier transformation has been applied to the recorded velocity. It can be seen that a peak at 555 kHz dominates the frequency domain of the recorded velocity. It is interesting to remark that there is not just one single radial mode but a combination of many of them with slightly different frequencies. This effect can be observed in the velocity response shown in Fig. 13(a), in which several peaks spaced by $\sim 100\text{--}130$ μ s are present. This is the typical shape of an amplitude modulated wave, also known as a “beat” in acoustics. This can also be observed in the Fourier transformation in Fig. 14(a), in which the peak at 555 kHz is not isolated but surrounded by components from 540 to 550 kHz. The origins of these different waves with slightly different frequencies are related to the intrinsic generation of the radial modes, as this modulation also appears in simulations, even when assuming an infinitely elastic material, as well as in numerical modal analyses presented in Ref. [27].

Similarly as in the Fourier analysis shown in Fig. 14(a), Fig. 15 shows the high-frequency domain of the recorded velocity at low-intensity pulses for the seven irradiated materials. It can be seen that the period corresponding to the dominant radial wave (1.8 μ s for the case of Mo and TZM) changes for each of the irradiated materials depending on the speed of sound through them. These experimental measurements are fully consistent with the ones analytically predicted for the “planar radial vibration mode”,

even though such analytic predictions are done under the assumption of elastic material, zero shear stress and strain, and uncoupling the longitudinal and radial vibration [27].

Figures 16–18 show the displacement response in the T2-TZM1 target for the same low-intensity pulse as shown in Fig. 13, obtained from the integration of the measured velocity. In Fig. 16, which shows the recorded displacement during 3 ms after the beam impact, it can be seen that the response is composed by three clearly differentiated waves: (i) a low-frequency wave with a period of ~ 1.64 ms identified as an excited bending mode, (ii) a wave with a period of ~ 86 μ s shown in the enlarged Fig. 17 and identified as a longitudinal mode, and (iii) a high-frequency wave with a period of ~ 1.82 μ s shown in the enlarged Fig. 18 and identified as the radial mode.

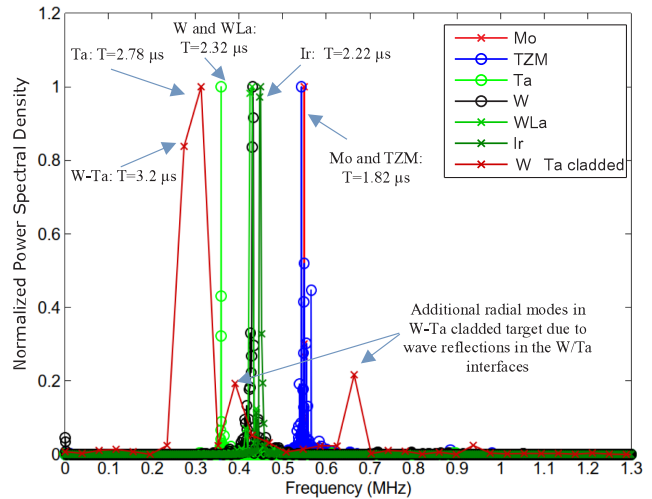


FIG. 15. Summary plot of the frequency domains of the surface velocity recorded at low-intensity pulses for the seven irradiated materials. Different periods of the recorded dominant radial mode consistent with the different speeds of sound in each material can be observed.

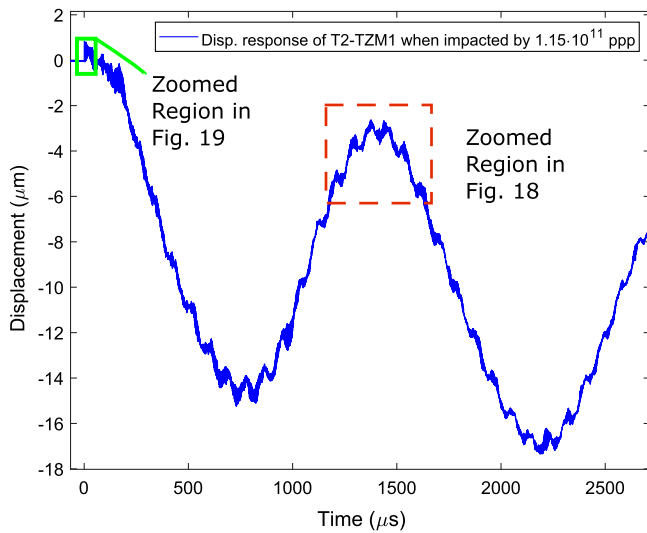


FIG. 16. Displacement response recorded by the LDV when impacting T2-TZM1 with 1.15×10^{11} ppp. Bending mode waves, longitudinal waves, and radial waves can be identified.

The large-amplitude and low-frequency wave shown in Fig. 16 has been recorded for all the irradiated targets at all the intensities (with some changes in the period when increasing the intensity). The recording of this wave was not foreseen during the design phase of the experiment. Its origin is the excitation of a bending mode caused by small offsets in the beam impact position. These bending modes appearing in rods impacted by proton beams have been identified and described previously in the literature (Ref. [28]). However, in that study the authors considered much larger off-axis impacts (60% of the radius) compared with the high levels of accuracy in the beam impacts achieved in this experiment (maximum eccentricities were

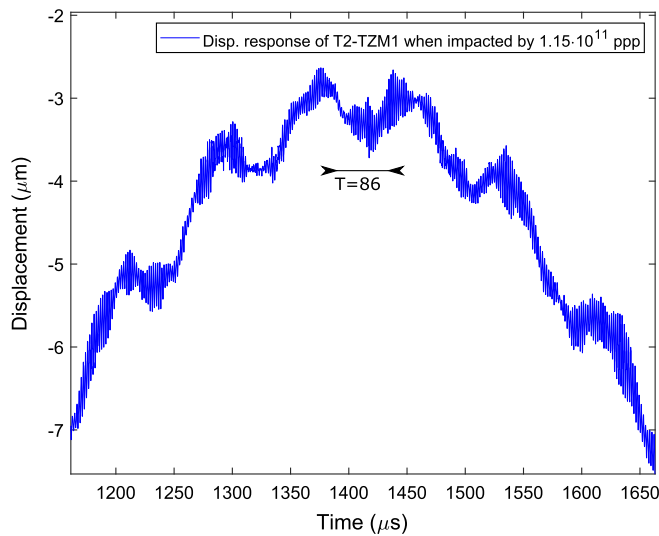


FIG. 17. Enlargement of the displacement response shown in Fig. 16 in the time window of 1200–1600 μ s showing the 86 μ s period longitudinal wave.

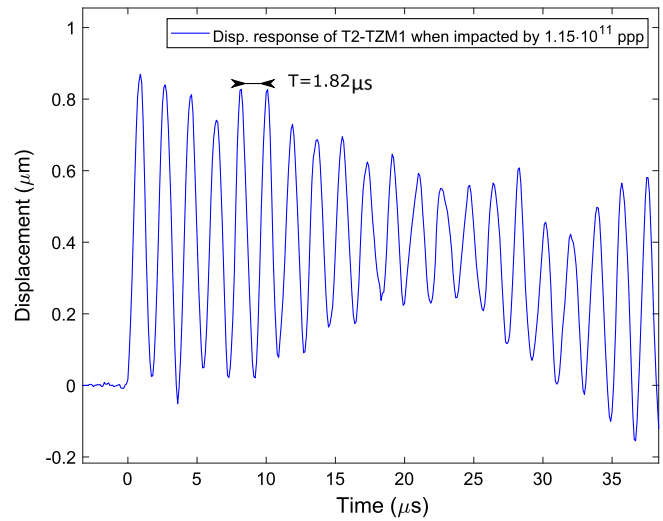


FIG. 18. Enlargement of the displacement response shown in Fig. 16 during the first 35 μ s after the beam impact, showing the 1.82 μ s period radial wave.

on the order of 0.4 mm which are less than 10% of the radius). It seems, however, that even with a high level of accuracy, small offsets and asymmetries caused by the clamping system were enough to excite it [27]. In addition, this bending mode is a strong candidate to explain the large levels of bending and deformations observed in all the targets at the end of the experiment. This aspect will be described in detail in a further publication covering the PIEs and the numerical simulation cross-checks of the experiment.

As previously stated, remarkable differences between the irradiated materials were observed even for the low-intensity pulses. Figure 19 shows the comparison between the velocity and the position response of the T2-TZM1

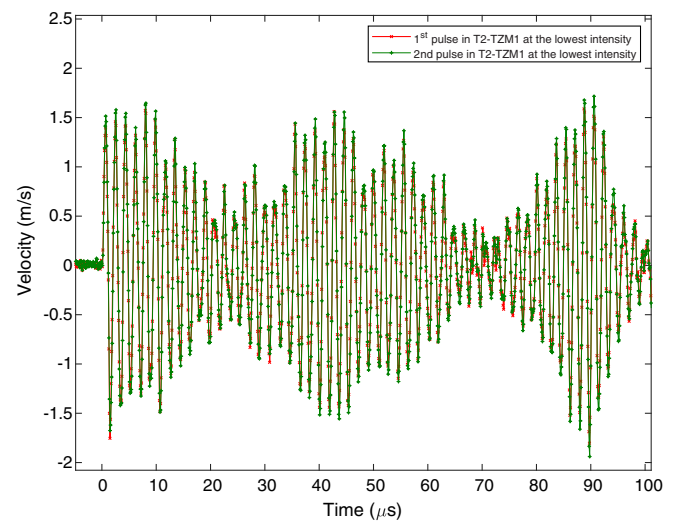


FIG. 19. Comparison between recorded responses of two consecutive impacted pulses on T2-TZM1 at the lowest intensity (1.15×10^{11} ppp) during the first 100 μ s.

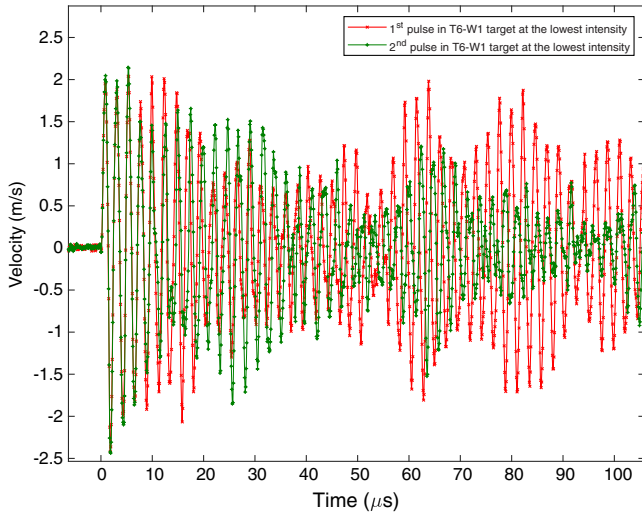


FIG. 20. Comparison between the recorded velocity of two consecutive impacted pulses on T6-W1 at the lowest intensity (1.09×10^{11} ppp) during the first 100 μs .

target when impacted by two successive low-intensity pulses (red dots represent the first pulse, while green dots represent the second one). It is very interesting to see that the response produced by two pulses is almost identical, with barely any shift in the frequency or in the velocity. This clearly indicates that the material responds elastically and the beam did not produce internal changes in the target yet. On the other hand, Fig. 20 shows a similar comparison between two consecutive low-intensity pulses but in a tungsten target. First of all, it is important to remark that the tungsten velocity response (Fig. 20) is very different from the one of TZM (Fig. 13), as the surface velocity of tungsten was rapidly damped before 1 ms. In addition, it can be observed in the comparison of the velocity between the first and the second impacted pulses that damping occurs even faster in the second one. Looking in detail at the first 20 μs after the pulse impact shown in Fig. 20, it

can be seen that a shift and a change of period of the radial wave takes place after a few oscillations. All these hints clearly indicate that the tungsten material is already experiencing plastic deformation even for low-intensity pulses (1.09×10^{11} ppp). In any case, a clear radial wave can still be identified, suggesting that significant internal cracking was not taking place yet.

B. Change of the dynamic response at medium intensities from $\sim 2 \times 10^{11}$ to $\sim 1 \times 10^{12}$ ppp

Figures 21(a)–21(c) show the velocity responses measured by the LDV when three consecutive pulses of 2.11×10^{11} ppp (second irradiation intensity) were impacted in (a) tungsten and (b) iridium and $\sim 5 \times 10^{11}$ ppp in (c) TZM. These plots show the velocity only during the first 20–50 μs after the impact, since after this time the velocity is almost completely damped. It can be observed how the response in the targets radically changes compared to the ones at the lowest intensities shown in Figs. 19 and 20, where damping was taking place significantly later.

In addition, it is very interesting to observe how the maximum velocity reached in the tungsten target progressively decreases in each consecutive pulse, reaching a maximum value of 4 m/s in the third pulse, while in the first one it reached 6 m/s. This could clearly indicate internal damage and cracking in the target material. This hypothesis is supported by the response predicted by simulations when assuming a failure model, as it was introduced in Fig. 5(b).

The iridium target [Fig. 21(b)] behaves better than the tungsten, but in any case the way the radial wave starts to be distorted can be observed, in particular, after some initial oscillations during the third consecutive impacted pulse. It is important to note at this point that the conditions reached at these intensities in W and Ir are still several times lower than the ones reached in the real AD target. For example, the impacted intensity of 2.11×10^{11} ppp with the measured beam size is estimated to produce an

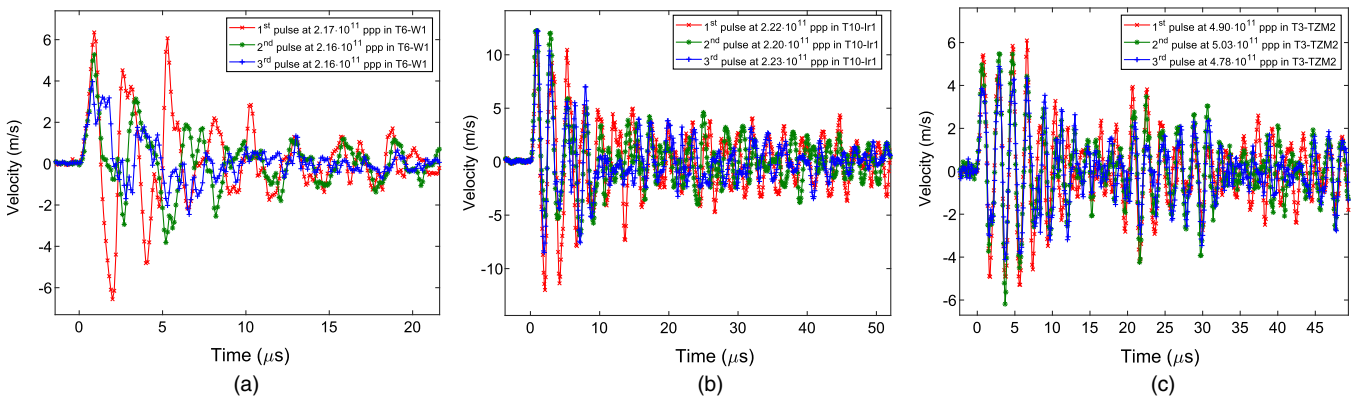


FIG. 21. Velocity response at the target surface for three consecutively impacted pulses of $\sim 2.1 \times 10^{11}$ ppp in (a) tungsten and (b) iridium and (c) $\sim 5 \times 10^{11}$ ppp in TZM. Progressive distortion of the radial wave at these conditions suggests the appearance of internal cracks in these materials.

adiabatic temperature rise on the order of 700°C (in comparison with the 2000°C estimated in the AD target) and tensile pressures of -1 GPa (in comparison with the -5 GPa of the AD target). Distortion of the radial wave in the TZM targets also took place when impacting consecutive pulses of $\sim 5 \times 10^{11}$ ppp (3 times less demanding conditions than reached in the real AD target) as shown in Fig. 21(c). The estimated rise of temperature in the TZM impacted by this intensity is on the order of 450°C and the associated tensile pressures on the order of 500 MPa .

On the other hand, Fig. 22 shows the velocity response of one of the tantalum targets impacted by 4.95×10^{11} ppp. Tantalum is without doubt the target that, at least from a dynamic point of view, behaved the best during the experiment. It can be seen that, while the rest of the target materials responded with a quick distorted damping of the radial waves when increasing the intensity above 2.2×10^{11} ppp, tantalum still presented a clean radial wave at 4.95×10^{11} ppp, showing a nondistorted radial wave even $300\ \mu\text{s}$ after the beam impact, as illustrated in the enlarged Fig. 22(b). The estimated maximum temperature and tensile pressure reached during these medium-intensity pulses in Ta are 900°C and -1.9 GPa , respectively. It is true that the tantalum targets were certainly experiencing plastic deformation, probably even from the first intensity, due to its low yield strength (definitely well below 80 MPa at these temperatures). Nevertheless, this yielding phenomenon does not seem to have an effect on the radial mode generation, and, differently from what happens in the rest of the materials, it does not distort it nor does it change its frequency, suggesting the absence of internal cracking.

C. Dynamic response at AD-target conditions $\sim 1.6 \times 10^{12}$ ppp

Figures 23(a), 23(b), and 24 show the recorded velocity at AD-target conditions for the T9-WLa, T2-TZM1, and T4-Ta1 targets, respectively. As can be observed in the figures, the recorded response for T9-WLa and T2-TZM1 shows a completely distorted radial wave which damps in a few oscillations. The responses of the pure tungsten and iridium targets at these conditions were similar and are not presented here. The high extent of wave distortion in these materials suggests a considerable presence of internal cracks, confirming the predictions of the hydrocode simulations of Ref. [3].

The tantalum target, on the other hand, still presented a clear radial wave at these conditions as shown in Fig. 24. The rise of temperature in Ta associated to this pulse is estimated on the order of 1700°C , with tensile pressures exceeding 4 GPa . This is probably the most remarkable result of the present work, which indicates that tantalum may be the best candidate material for the future AD-target core.

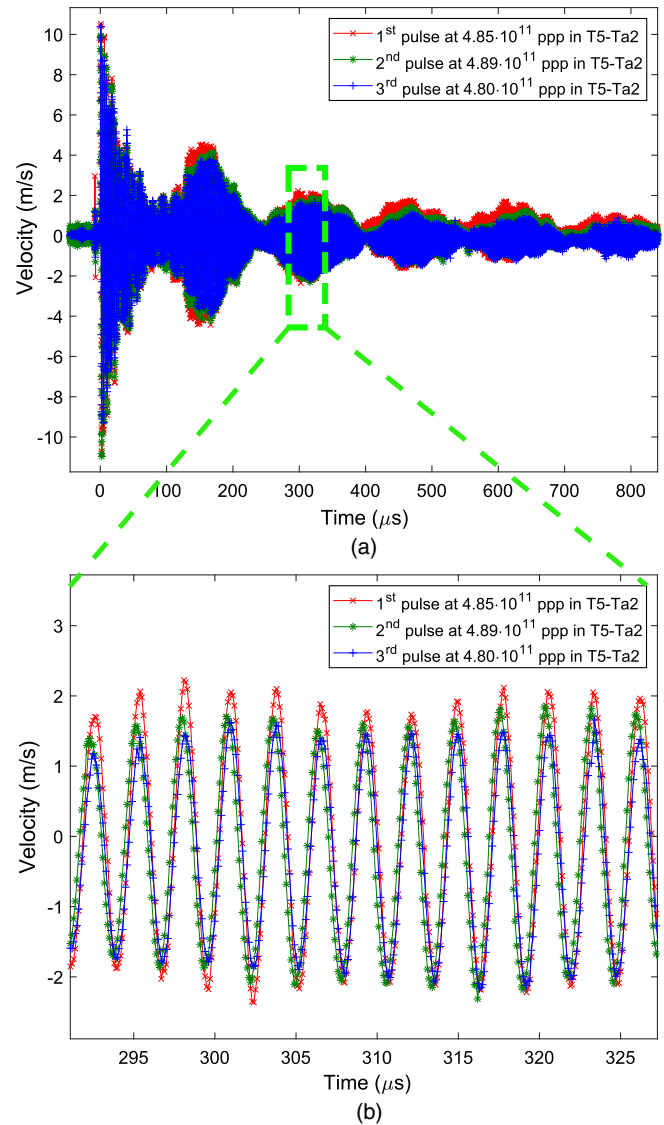


FIG. 22. (a) Velocity response at the T5-Ta2 target surface for three consecutively impacted pulses of $\sim 5 \times 10^{11}$ ppp during $800\ \mu\text{s}$ after the impact. (b) Enlarged plot of the $290\text{--}330\ \mu\text{s}$ time window showing clear and repeatable radial waves for the three consecutively impacted pulses.

In addition, a particular pulse case is discussed in this subsection corresponding to the proton beam pulse at the maximum intensity, 1.71×10^{12} ppp, impacted onto the T12-Ir3 iridium target which was left virgin until the end of the experiment as introduced in Table III. The interesting aspect of this case is that this target had not been exposed previously to any other impact which would have already produced changes in the material. Therefore, this could be the most representative testing conditions for the real AD-target response. Figure 25 shows the state of the T12-Ir3 target after a single beam impact at this intensity, indicating an impressive response very different from the impacts in all the other targets. The target was massively fragmented

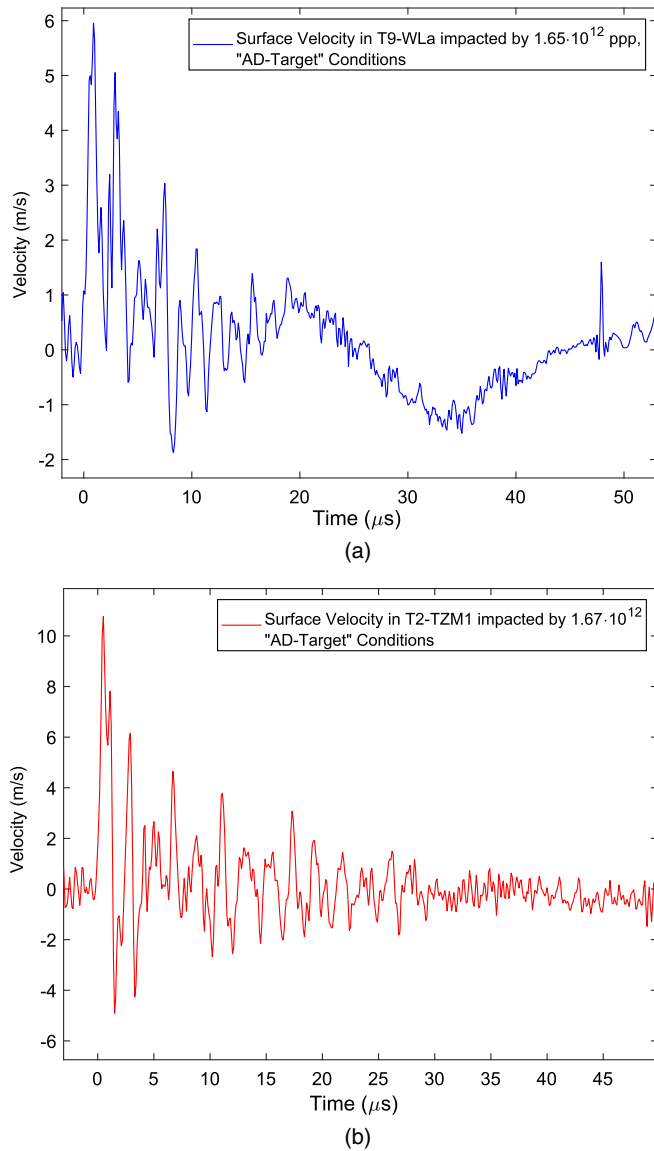


FIG. 23. Surface velocity recorded on targets T9-WLa and T2-TZM1, respectively, at AD-target conditions.

following a bulb shape, which is consistent with the longitudinal profile of deposited energy in the target shown in Fig. 3. This mode of failure is probably caused by the sudden and extensive internal cracking during the pulse impact, causing the inertia of the expansion to rapidly propagate these cracks towards the target surface, resulting in the observed target splitting in longitudinal filaments. The potential melting of the core of the target is not believed to be the reason of this fracture, since simulations with the real beam parameters of this impact showed that the maximum temperature reached was only 2000 °C (the melting point of iridium is 2450 °C). In addition, postirradiation examinations of the core material by microscope did not show any trace of material melting in the microstructure.

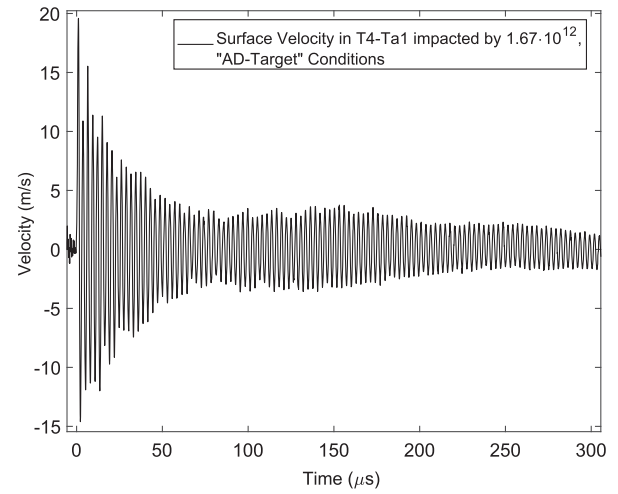


FIG. 24. Recorded surface velocity in the T5-Ta2 target after being impacted by a pulse of 1.67×10^{12} ppp (AD-target conditions). It can be seen that the generated radial wave is still clear and undistorted. This is probably one of the most important findings of the experiment.

D. Summary of response of all the irradiated targets

A results summary is carried out by showing specific quantitative information extracted from each single impact and plotting it as a function of the impacted intensity. Figure 26 shows the maximum surface velocity recorded by the LDV OptoMET® for each single pulse impacted for the seven types of materials irradiated. Normally, this maximum velocity is reached during the first radial oscillation after the pulse impact; therefore, it is a good indicator of the material’s state and of the level of internal damage suggested by the distorted and damped radial response (previously discussed in Sec. IV B).

In the absence of failure, one would expect a monotonic increase of velocity with the impacted intensity and higher velocities with denser materials, while in reality this was not the case due to internal damage in the target materials. Important differences in the response can be observed. For example, it is certainly clear that tungsten (light green) was experiencing important damage from the second irradiation intensity, at 2.17×10^{11} ppp, associated to a rise of temperature on the order of 700 °C, with tensile pressures of



FIG. 25. Picture of the state of the T12-Ir3 target after a single beam impact of 1.71×10^{12} ppp.

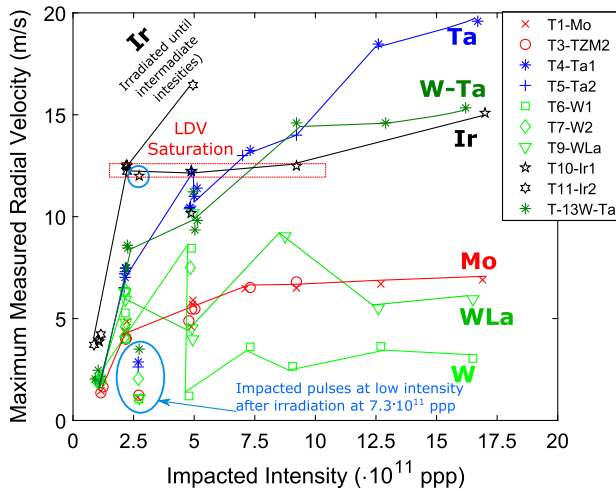


FIG. 26. Summary of maximum recorded surface velocity during the experiment for the irradiated materials. In the absence of failure, one would expect a monotonic increase of velocity with intensity and higher velocities with denser materials. This was not the case, and only Ta showed such behavior, suggesting its superior performance.

–1 GPa. It can be observed that during the subsequent impacted pulses at this intensity the tungsten targets presented low external velocities. In addition, in the next pulses at higher intensities, the maximum velocity reached was similar or even decreasing. The W-La target seems to have a slightly better behavior, since the reached velocities are higher. In any case, it is possible to observe a drop in the maximum reached surface velocity in this target when increasing the intensity. On the other hand, the Ta-cladded tungsten target seems to present a better response, showing a monotonic increase of maximum velocities up to 5×10^{11} ppp. Molybdenum and TZM targets show a similar response (somewhat better than W), reaching always almost the same maximum velocity when increasing the intensity above 5×10^{11} ppp, suggesting internal fracture from these conditions. The iridium targets presented very high velocities during the first pulses, causing the saturation of the instrument when these velocities were above 12.5 m/s. However, after its irradiation at 5×10^{11} ppp, it is possible to observe a large drop of the maximum reached velocity. Nevertheless, it is interesting to observe that iridium presented a better response than tungsten even if its density is 20% higher. Tantalum targets are the only ones in which externally reached velocities continued monotonically growing during the whole experiment, reinforcing what was observed looking at its “clean” and nondistorted dynamic response, which was present even at the highest intensity.

V. CONCLUSIONS

This work presented a detailed analysis of the most significant online results recorded during the 139 high-

intensity, 440 GeV, proton pulses impacted onto 13 targets of Ir, Mo, TZM, Ta, W, W-La, and W cladded in Ta. A large amount of online data of the target surface velocity, displacement, and temperatures was measured. The radial and longitudinal waves predicted by hydrocode simulations were recorded, in particular, at low-intensity pulses. A third lower-frequency wave was also recorded and identified as an excited bending mode resulting from a minor off-axis deviation of the proton impacts. In addition, it was possible to infer progressive alteration and damage in the target materials while increasing the impacted intensity by changes in the surface radial velocity of the targets recorded online.

The main outcome of the experiment is that most of the irradiated targets (all except tantalum) were suffering significant internal damage even from reached conditions 5–7 times lower than the ones taking place in the real AD target, indicating that the iridium core of that target may be seriously damaged and fragmented from the very beginning of operation. The predicted radial compressive-to-tensile wave studied in detail in Ref. [3] is confirmed to be the main damaging phenomena and probably the cause of the drop in antiproton production often observed during the first days of operation, since fragmentation of the target core may lead to the loss of its effective density and primary beam-target interaction.

The excellent response of tantalum in the experiment (which showed a nondistorted radial wave even at the highest-intensity pulses, therefore indicating the absence of internal cracks) makes it one of the most probable candidate materials for the future AD-target design. Based on this result, a first scaled prototype of the AD target equipped with a tantalum core has been manufactured and tested in HiRadMat, exposed to 50 high-intensity pulses (HRMT-42 experiment). A new type of failure in tantalum, identified as spalling, has been observed during this irradiation, and it is currently under investigation. Details are discussed in Ref. [29].

Nevertheless, the identification of the radial compressive-to-tensile wave as the main short-term damaging phenomenon shown in the present study (as well as the recent discoveries in Ref. [29]) motivates the pursuit of strategies to mitigate the effect of this wave in the new target design, such as relaxation of beam primary optics or changes in the target core geometry, while remaining compatible with physics requirements.

Detailed postirradiation examinations will complement the online results presented here. In addition, experimental versus simulation cross-checks will be included, assessing the validity of the used hydrocodes material models as well as the origin of the unforeseen bending mode excitation observed in the displacement response.

ACKNOWLEDGMENTS

The authors express their gratitude to the HiRadMat facility for its invaluable support during the design and

execution of the experiment as well as to all the CERN groups involved, such as BE/OP/SPS, BE/BI/PM, HSE/RP/AS, and EN/MME. In addition, the authors thank CERN's Accelerator Consolidation (ACC-CONS) Project, which financed this work, as well as the funding received through the EuCARD2 FP7 program (Grant Agreement No. 312453) in the context of the HiRadMat facility. Finally, the authors are grateful to Anna Lambert and Louisa Catherall for the English proofreading of this manuscript.

-
- [1] D. Möhl, Production of low-energy antiprotons, *Hyperfine Interact.* **109**, 33 (1997).
- [2] M. R. Bellone, G. del Torre, M. Ross, and P. Sievers, The design and prototype test of the CERN antiproton production target, Technical Report No. SPS/80-9/ABT, CERN, Geneva, 1980.
- [3] C. Torregrosa, A. Perillo-Marcone, M. Calviani, and J.-L. Muñoz Cobo, CERN antiproton target: Hydrocode analysis of its core material dynamic response under proton beam impact, *Phys. Rev. Accel. Beams* **19**, 073402 (2016).
- [4] B. Hopkinson, A method of measuring the pressure produced in the detonation of high explosives or by the impact of bullets, *Phil. Trans. R. Soc.* **213**, 437 (1914).
- [5] M. Scapin, L. Peroni, C. Torregrosa, A. Perillo-Marcone, L. Gomez M. Calviani, F. Leaux, and M. Meyer, Experimental results and strength model identification of pure iridium, *Int. J. Impact Eng.* **106**, 191 (2017).
- [6] I. Efthymiopoulos, C. Hessler, H. Gaillard, D. Grenier, M. Meddahi, P. Trilhe, A. Pardons, C. Theis, N. Charitonidis, S. Evrard, H. Vincke, and M. Lazzaroni, Hiradmat: A new irradiation facility for material testing at CERN, in *Proceedings of the 2nd International Particle Accelerator Conference, San Sebastián, Spain* (EPS-AG, Spain, 2011), pp. 1665–1667.
- [7] A. Ferrari, P. R. Sala, A. Fasso, and J. Ranft, FLUKA: A multi-particle transport code (Program version 2005), CERN Reports No. CERN-2005-010, No. SLAC-R-773, and No. INFN-TC-05-11, 2005.
- [8] G. R. Johnson and W. H. Cook, *A Constitutive Model and Data for Metals Subjected to Large Strains, High Strain Rates and High Temperatures* (The Hague, Netherlands, 1983).
- [9] SCHOTT AG, Tie-42 radiation resistant optical glasses, Technical Report, 2007, https://www.schott.com/d/advanced_optics/0bdd65d7-4d93-4d35-927a-a22fc6044d8e/1.4/schott_tie-42_radiation_resistant_optical_glasses_row.pdf.
- [10] T. Bogey and R. Jones, The beam position system of the CERN neutrino to grand sasso proton beam line, in *Proceedings of DIPAC, Venice, Italy, 2007* (DIPAC, 2007), <https://accelconf.web.cern.ch/accelconf/d07/papers/tupb31.pdf>.
- [11] E. Bravin, S. Burger, G. F. Ferioli, G. Focker, and A. Guerrerro, A new tv beam observation system for CERN, in *Proceedings of DIPAC, 2005* (DIPAC, 2005).
- [12] Cid8825d color radiation hardened camera, <https://www.thermofisher.com/order/catalog/product/CID8825D>.
- [13] Full hd wdr day/night fixed network camera dcs-3716, D-Link, <http://www.dlink.com/uk/en/business-solutions/ip-surveillance/business-ip-cameras/box-cameras/dcs-3716-full-hd-wdr-poe-day-night-fixed-camera>.
- [14] Goodfellow Ltd., <http://www.goodfellow.com/>.
- [15] M. Rieth *et al.*, Review on the EFDA programme on tungsten materials technology and science, *J. Nucl. Mater.* **417**, 463 (2011).
- [16] J. W. G. Thomason, Upgrades to isis for the new second target station, in *Proceedings of the 11th European Particle Accelerator Conference, Genoa, 2008* (EPS-AG, Genoa, Italy, 2008).
- [17] S. Peggs and R. Kreier, C. Carlile, R. Miyamoto, A. Paahlsson, M. Trojer, and J. G. Weisend II., ESS Technical design report, Technical Report No. ESS-doc-274, 2013.
- [18] M. Anelli *et al.* (SHiP Collaboration), A facility to Search for Hidden Particles (SHiP) at the CERN SPS, CERN Reports No CERN-SPSC-2015-016 and No. SPSC-P-350, 2015.
- [19] M. Mabuchi, K. Okamoto, N. Saito, M. Nakanishi, Y. Yamada, T. Asahina, and T. Igarashi, Tensile properties at elevated temperature of w-la2o3, *Mater. Sci. Eng. A* **214**, 174 (1996).
- [20] Mechanical properties of pure tungsten, PLANSEE Web page.
- [21] C. Torregrosa, A. Perillo-Marcone, and M. Calviani, Designs characteristics and main inherent concerns of the antiproton decelerator target, CERN Technical Report No. CERN-ACC-NOTE-2015-0004, 2015, <https://cds.cern.ch/record/1993542?ln=en>.
- [22] S. Nemat-Nasser, J. B. Isaacs, and M. Liu, Microstructure of high-strain, high-strain-rate deformed tantalum, *Acta Mater.* **46**, 1307 (1998).
- [23] W. R. Thissell, D. L. Tonks, D. Schwartz, and J. House, Dynamic failure resistance of two tantalum materials with different melt practice sequences, *AIP Conf. Proc.* **706**, 495 (2003).
- [24] S. V. Razorenov, G. Garkushin, G. I. Kanel, and O. N. Ignatova, The spall strength and Hugoniot elastic limit of tantalum with various grain size, *AIP Conf. Proc.* **1426**, 991 (2012).
- [25] F. F. Schmidt and H. R. Ogden, Defense Metal Information Center, The engineering properties of tantalum and tantalum alloys, DMIC Technical Report No. 189, 1963.
- [26] P. Abenthung, Product specification tam rod, Plansee Technical Report No. PS-MPR-112, 2014, https://www.plansee-com.azureedge.net/fileadmin/user_upload/PLANSEE_Specification_Tantalum_rod_09.12.pdf.
- [27] N. Solieri and C. Torregrosa, Dynamic studies of multiple configurations of CERN Antiproton Decelerator Target core under proton beam impact, 2017, <http://cds.cern.ch/record/2310189?ln=en>.
- [28] A. Dallochio, Ph.D. thesis, Politecnico di Torino, Torino, 2008.
- [29] C. T. Martin, M. Calviani, A. Perillo-Marcone, R. Ferriere, N. Solieri, M. Butcher, L.-M. Grec, and J. C. Espadanal, Scaled prototype of a tantalum target embedded in expanded graphite for antiproton production: Design, manufacturing, and testing under proton beam impacts, *Phys. Rev. Accel. Beams* **21**, 073001 (2018).